III-V Diode Lasers for New Emission Wavelengths

H.K. Choi, C.A. Wang, and S.J. Eglash

■ Two types of III-V diode lasers have been developed for new emission wavelengths. We have obtained emission at 0.9 to 1.06 μm from quantum-well lasers with a strained InGaAs active layer and AlGaAs confining layers. Organometallic vapor phase epitaxy (OMVPE) was used to grow the layers on GaAs substrates. These InGaAs/AlGaAs lasers have achieved threshold current densities as low as 65 A/cm^2, differential quantum efficiencies as high as 90%, and, for devices 300 μm wide and 1000 μm long, continuous output powers up to 3.2 W and power efficiencies as high as 47%.

We have obtained emission at 2.27 μm from lattice-matched double-heterostructure lasers with a GaInAsSb active layer and AlGaAsSb confining layers grown by molecular-beam epitaxy (MBE) on GaSb substrates. These GaInAsSb/AlGaAsSb lasers have exhibited threshold current densities as low as 1.5 kA/cm^2, differential quantum efficiencies as high as 50%, and pulsed output powers as high as 1.8 W. These efficiencies and power values are the highest ever reported for room-temperature operation of semiconductor lasers with emission wavelengths >2 μm. Emission from 1.8 to 4.4 μm can potentially be achieved by changing the GaInAsSb composition.

Semiconductor diode lasers have been highly successful because they are very efficient, compact, reliable, and suitable for economical mass production. The availability of these lasers has created many new applications in, among other areas, fiber optic communications, compact-disc players, optical memory drives, laser printers, and laser-pumped solid state lasers. The different applications generally require different emission wavelengths. For example, fiber optic communications currently require wavelengths of 1.3 or 1.55 μm because silica-based optical fibers have zero chromatic dispersion at 1.3 μm and their lowest loss at 1.55 μm. For high-density optical memories, fast laser printers, and bar-code readers, visible emission is very advantageous because of the short wavelength. The optical pumping of lasers made from Nd:YAG (a neodymium-doped garnet comprised of yttrium, aluminum, and oxygen) is an application that requires emission close to 0.808 μm to match the strongest Nd^{+3} absorption band.

A diode laser basically consists of an active layer where photons are generated by carrier recombination, and confining layers with a lower refractive index and higher bandgap, which serve to confine the light and carriers. Epitaxial techniques are used to grow the layers on a single-crystal substrate. For an individual laser, the photon energy—and thus the emission wavelength—is limited to a narrow range determined mainly by the bandgap energy of the material forming the active layer. In commercial diode lasers that are used for room-temperature applications such as those mentioned earlier, the substrate is either InP or GaAs, and the active and confining layers are III-V alloys that are lattice matched to the substrate. For the three principal types of lasers currently available, the layer and substrate materials and the range of emission wavelengths are, respectively,

- $In_{1-x}Ga_xAs_yP_{1-y}/InP$ (by convention, the active layer is listed first and the confining layers second) on InP, 1.1 to 1.67 μm;
- $Al_xGa_{1-x}As/Al_yGa_{1-y}As$ on GaAs, 0.7 to 0.9 μm; and
- $(Al_xGa_{1-x})_{0.5}In_{0.5}P/(Al_yGa_{1-y})_{0.5}In_{0.5}P$ on GaAs, 0.63 to 0.67 μm.

For each type of laser, different emission wavelengths in the specified range can be obtained by changing the alloy composition of the active layer.

This article describes InGaAs/AlGaAs and GaInAsSb/AlGaAsSb diode lasers developed at Lincoln Laboratory for emission at wavelengths not available commercially. Like commercial devices, the two new types of lasers use III-V alloys for the active and confining layers.

The InGaAs/AlGaAs lasers are similar in structure to AlGaAs/AlGaAs graded-index separate-confinement-heterostructure single-quantum-well (GRIN-SCH SQW) devices [1]. In an InGaAs/AlGaAs laser, however, the lattice-matched AlGaAs active layer is replaced by an $In_xGa_{1-x}As$ layer that is under strain because its lattice constant is significantly greater than that of the AlGaAs confining layers. Such strained-layer InGaAs/AlGaAs lasers are under development at many laboratories. Incorporation of In in the active layer enables the extension of the emission to wavelengths longer than those produced by AlGaAs/AlGaAs devices. By varying the x value of the $In_xGa_{1-x}As$ layer from 0.02 to 0.3, we have obtained emission at wavelengths from 0.9 to 1.06 μm. The operating characteristics of our InGaAs/AlGaAs lasers are equal or superior to those of similar devices fabricated elsewhere, as well as to those of AlGaAs/AlGaAs lasers. We have used InGaAs/AlGaAs lasers that emit at 0.94 or 0.97 μm to pump Yb:YAG lasers emitting at 1.03 μm [2], while InGaAs/AlGaAs lasers that emit at 0.98 μm have been used to pump Er-doped silica-fiber amplifiers operating at 1.53 μm [3].

The GaInAsSb/AlGaAsSb lasers, which are at a much earlier stage of development than the InGaAs/AlGaAs devices, use a double heterostructure in which both the active and confining layers are lattice matched to a GaSb substrate. By using an active-layer composition of $Ga_{0.84}In_{0.16}As_{0.14}Sb_{0.86}$, we have obtained emission at 2.27 μm. Emission wavelengths from 1.8 to 4.4 μm can potentially be obtained for the range of GaInAsSb compositions that are lattice matched to GaSb. Possible applications of GaInAsSb/AlGaAsSb lasers include optical communications that employ low-loss fluoride fibers (the theoretical loss is 0.01 dB/km at 2.55 μm [4], compared with 0.2 dB/km for silica-based fibers), laser radars that exploit atmospheric transmission windows, remote sensing of atmospheric gases, and molecular spectroscopy.

InGaAs/AlGaAs Strained-Layer Quantum-Well Lasers

Figure 1 shows the bandgap versus lattice constant for AlGaAs and InGaAs alloys. Note that AlGaAs is almost lattice matched to GaAs over the entire composition range. InGaAs, however, cannot be lattice matched to GaAs because the lattice constant of $In_xGa_{1-x}As$ increases linearly with x from 0.5653 nm for GaAs to 0.6058 nm for InAs. For that range of x, the bandgap of $In_xGa_{1-x}As$ at room temperature decreases from 1.424 eV for GaAs to 0.35 eV for InAs according to the following equation [5]:

$$E_g(x) = 1.424 - 1.614x + 0.54x^2 .$$

InGaAs/AlGaAs lasers are the first successful lasers with an active layer that is not lattice matched to the substrate. The quality of lasers that incorporate lattice-mismatched layers has generally been poor because such layers have had a high density of dislocations. Dislocation formation can be avoided, however, by limiting the InGaAs to a sufficiently thin active layer while keeping the lattice-matched AlGaAs in thick cladding layers. In this design, the thin InGaAs layer is elastically strained (see the box, "The Concept of Strained Layers").

The first InGaAs/AlGaAs lasers were reported by

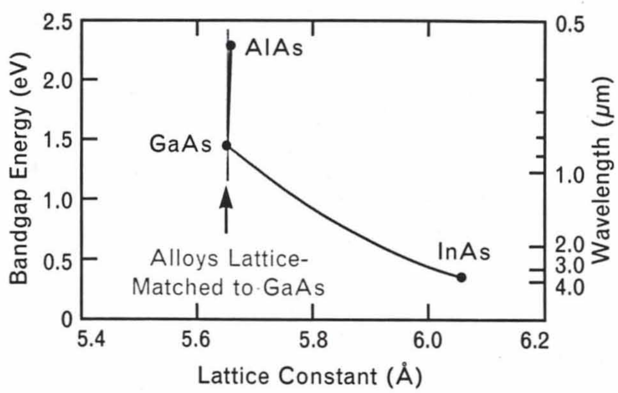

FIGURE 1. Bandgap energy versus lattice constant for AlGaAs and InGaAs.

W.T. Tsang in 1980 [6]. By incorporating as much as 4.5% In, Tsang extended the emission wavelength to 936 nm. Other reports of InGaAs/AlGaAs lasers followed [7, 8], but these devices were not very stable because the thicknesses of the active layers exceeded the critical value for dislocation formation. The first stable strained-layer laser was reported by D. Fekete et al. in 1986 [9]. Subsequently, many groups have reported InGaAs/AlGaAs strained-layer lasers with better characteristics [10–17].

In our investigation of InGaAs/AlGaAs lasers, we have varied the laser structural parameters to optimize these parameters and to understand their effects on laser properties. In evaluating laser performance, we have focused on two characteristics: threshold current density J_{th} and differential quantum efficiency η_d, both of which can be derived from the measured curve of output power P versus current I. The threshold current is defined as the current at which the gain from the laser becomes equal to the cavity loss and above which the light output increases rapidly. The value of J_{th} is equal to the threshold current divided by the cross-sectional area of the laser active region. The differential quantum efficiency measures the increase in the number of photons emitted by the laser per electron-hole pair injected into the active layer. The value of η_d is obtained from the slope of the P-I curve above threshold. Lower values of J_{th} and higher values of η_d are preferable; such values reduce the current density required to attain a given laser power. We have achieved the lowest value of J_{th} and highest value of η_d thus far reported for InGaAs/AlGaAs lasers.

Structure and Epitaxial Growth

Figure 2 is a schematic diagram of the GRIN-SCH SQW laser. Laser light is generated in the thin $In_xGa_{1-x}As$ quantum-well active layer. The $Al_yGa_{1-y}As$ GRIN confining layers, in which the y value increases linearly from a low value near the active layer to 0.7 away from the active layer, and the $Al_{0.7}Ga_{0.3}As$ cladding layers together establish a waveguide to confine the optical field. To improve the interface quality and laser characteristics, we include thin GaAs layers (discussed later) that bound the InGaAs active layer. Such bounding is not used in $Al_xGa_{1-x}As/Al_yGa_{1-y}As$ lasers.

We grew the laser structure on Si-doped n^+-GaAs

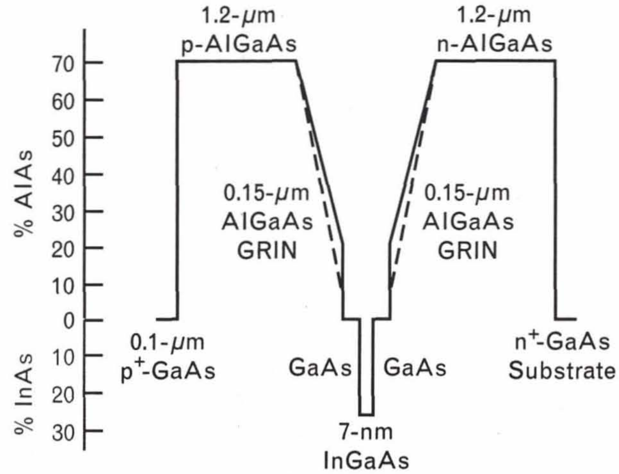

FIGURE 2. Schematic structure of InGaAs/AlGaAs graded-index separate-confinement-heterostructure single-quantum-well (GRIN-SCH SQW) diode laser.

substrates by using organometallic vapor phase epitaxy (OMVPE) in a low-pressure vertical rotating-disk reactor [1]. In OMVPE, the pyrolysis of gaseous OMs and hydrides is used to deposit epitaxial layers (epilayers) on a heated single-crystal substrate. The deposition of $In_xGa_{1-x}As$ and $Al_yGa_{1-y}As$ proceeds by means of the following reactions:

$$x\mathrm{In(CH_3)_3} + (1-x)\mathrm{Ga(CH_3)_3} + \mathrm{AsH_3} \rightarrow \mathrm{In}_x\mathrm{Ga}_{1-x}\mathrm{As} + 3\mathrm{CH_4},$$

and

$$y\mathrm{Al(CH_3)_3} + (1-y)\mathrm{Ga(CH_3)_3} + \mathrm{AsH_3} \rightarrow \mathrm{Al}_y\mathrm{Ga}_{1-y}\mathrm{As} + 3\mathrm{CH_4}.$$

The flow of a small amount of H_2Se or $Zn(CH_3)_2$ dopes the layer n- or p-type, respectively. On the basis of surface morphology and photoluminescence studies on test layers, we selected growth temperatures of 800°C for the AlGaAs layers and 640°C for the InGaAs layer. The large difference between these temperatures required that growth be interrupted for periods of several minutes before (after) the InGaAs growth to cool (heat) the substrate. The lower and upper GaAs bounding layers were grown during the cooling and heating periods, respectively.

Laser Characteristics

We grew a series of laser structures with variations in

THE CONCEPT OF STRAINED LAYERS

WHEN WE GROW an epilayer on a substrate that has a different lattice constant, the misfit is accommodated either by strain or by the generation of dislocations. If the epilayer is thin enough, strain is favorable from an energy standpoint and no dislocations are generated. The high quality of the strained layer allows the fabrication of high-performance devices.

As early as 1949, F.C. Frank and J.H. van der Merwe [1] considered the accommodation of misfit across the interface between a thin epilayer and its substrate. It was not until 1976, however, that J.W. Matthews and A.E. Blakeslee [2] grew the first strained layer (GaAsP on a GaAs substrate), and only recently that researchers have investigated the device applications of the strained-layer concept.

The critical thickness, below which a lattice-mismatched layer is strained, depends on the mechanical properties of the epilayer material and the degree of mismatch. Figure A plots the critical thickness for $In_xGa_{1-x}As$ on GaAs (or AlGaAs) as calculated by the model of Matthews and Blakeslee [3]. As x increases, the mismatch increases, and the critical thickness rapidly decreases. The thickness of the active layer in a diode laser is limited to the critical thickness because the dislocations present in thicker layers will significantly degrade both the optical and electrical characteristics.

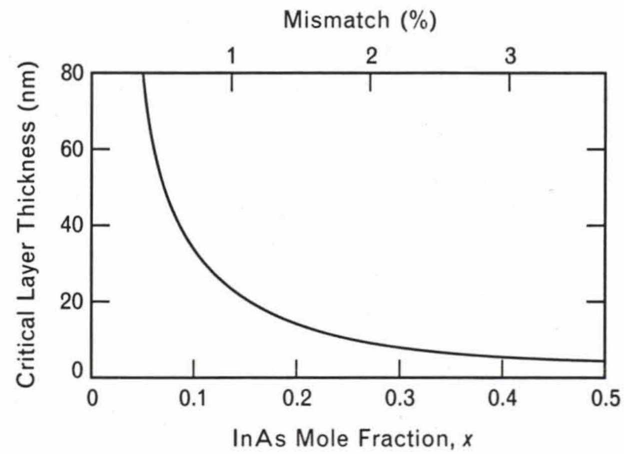

FIGURE A. Critical layer thickness of $In_xGa_{1-x}As$ layers on GaAs substrates as a function of x. (Note: Because AlGaAs has almost the same lattice constant as GaAs, the figure also applies to $In_xGa_{1-x}As$ layers on thick AlGaAs layers.)

Figure B schematically compares the two cases in which the epilayer thickness is respectively below and above the critical thickness. In a strained layer (Figure B[1]), the lattice constant in the direction parallel to the interface approximately matches that of the substrate. For InGaAs on GaAs, the epilayer is under in-plane biaxial compression. In the direction normal to the interface, the epilayer is elongated so that the lattice becomes tetragonal

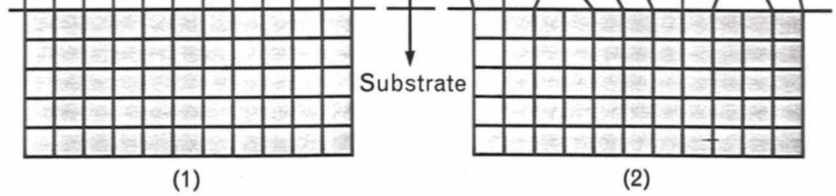

FIGURE B. Schematic diagram showing the lattice of (1) a strained layer, which is thinner than the critical thickness, and (2) a relaxed layer, which is thicker than the critical thickness.

rather than cubic. When the critical thickness is exceeded, misfit dislocations are generated at the growth interface and propagate back to the substrate-epilayer interface (Figure B[2]). Some of the dislocations are terminated by the formation of edge dislocations, but a considerable fraction of the dislocations propagates to the upper layer by threading. For a sufficiently thick layer, the lattice constant becomes equal to the bulk lattice constant, and the lattice is said to be fully relaxed.

The strain alters the structure of the energy bands, especially that of the valence bands. For a III-V semiconductor with a zinc-blende structure, Figure C compares the uppermost valence bands without strain and the same bands under biaxial compression. For the unstrained case, the heavy- and light-hole bands are degenerate at the Brillouin zone center. (The terms *heavy* and *light* denote a hole's effective mass, which is inversely proportional to d^2E/dk^2, where E denotes energy and k momentum. Note that d^2E/dk^2 is the curvature of the energy band.) The biaxial compression changes the band structure in three ways. First, the bandgap energy is increased. Second, the degeneracy at the Brillouin zone center is removed, and the separation between the heavy- and light-hole bands increases with strain. Finally, the valence bands become anisotropic. In the direction normal to the plane of the surface, the highest band has a heavy effective mass. In the parallel direction, however, the highest band has a light effective mass.

The change in the band structure of the strained layer has a significant implication for laser performance. In order to reach population inversion, the quasi-Fermi level must be separated by more than the bandgap energy. The number of carriers required to reach this condition is smaller for a smaller density of states. In quantum-well structures, the density of states is proportional to the effective mass in the parallel direction. Thus, because the effective mass in the parallel direction for compressively strained InGaAs is smaller than that for GaAs, we expect InGaAs/AlGaAs lasers to have lower threshold current densities than GaAs/AlGaAs lasers of a similar structure.

References

1. F.C. Frank and J.H. van der Merwe, "One-Dimensional Dislocations. II. Misfitting Monolayers and Oriented Overgrowth," *Proc. Roy. Soc. (London)* **A 198**, 216 (1949).
2. J.W. Matthews and A.E. Blakeslee, "Defects in Epitaxial Multilayers: III. Preparation of Almost Perfect Multilayers," *J. Cryst. Growth* **32**, 265 (1976).
3. J.W. Matthews and A.E. Blakeslee, "Defects in Epitaxial Multilayers: I. Misfit Dislocations," *J. Cryst. Growth* **27**, 118 (1974).

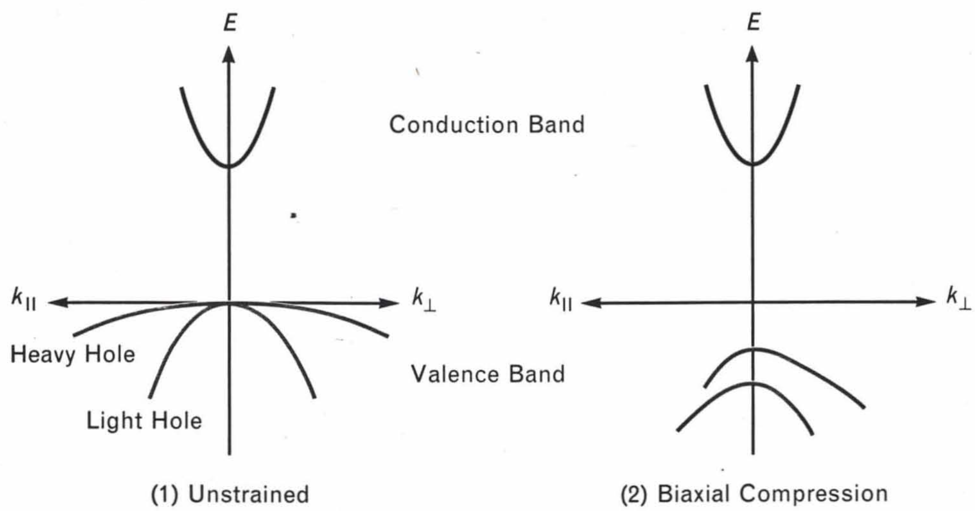

FIGURE C. Band structure of InGaAs near Brillouin zone center for the case of (1) no strain and (2) biaxial compression.

Table 1. Effect of GaAs Bounding-Layer Thickness *t* on the Characteristics of $In_{0.25}Ga_{0.75}As$/AlGaAs Diode Lasers

Wafer	t (nm)	J_{th} (A/cm^2)	λ (nm)	η_d (%)
A	—	550	970	46
B	5	150	1024	74
C	10	125	1022	80
D	15	130	1025	80

bounding-layer thickness t and InAs mole fraction x. Broad-stripe lasers either 100 or 300 μm wide were fabricated by the following procedure. A photolithographic lift-off process defined stripes of Ti/Au on the p^+-GaAs surface of a wafer. To reduce current spreading, we etched the p^+-GaAs layer and a part of the p-AlGaAs cladding layer from the areas between the stripes by immersing the wafer in a H_2SO_4:H_2O_2:H_2O solution. The wafer was then lapped to a thickness of ~100 μm, and the n-GaAs surface was metallized with Ge/Au/Ni/Ti/Au at 380°C in a H_2 atmosphere. Next, the wafer was cleaved into individual bars with cavity length L ranging from 300 to 1500 μm. Using a calibrated 1-cm-diameter Si photodiode detector, we measured the P-I curve of each laser in pulsed operation.

Effect of bounding layers. Lasers with L = 500 μm were fabricated from four wafers. Wafer A had no bounding layers (t = 0), while wafers B, C, and D had bounding layers with t = 5, 10, and 15 nm, respectively. Except for this variation in t, the wafers were identical, with x = 0.25, y = 0.2 to 0.7, and active-layer thickness d = 7 nm. The surface morphology was rough for wafer A, showed slight texture for wafer B, and was very smooth for wafers C and D. Table 1 summarizes the operating characteristics of the lasers. Note that lasers with t = 10 and 15 nm had almost the same characteristics: J_{th} = 125 and 130 A/cm^2, respectively, and η_d = 80%. The performance of lasers with t = 5 nm was slightly degraded, with J_{th} = 150 A/cm^2 and η_d = 74%. For the lasers without bounding layers, J_{th} rose sharply to 550 A/cm^2 and η_d fell to only 46%. In addition, the emission wavelengths shifted from ~1020 nm for lasers with bounding layers to ~970 nm for those without, as a result of the increase in J_{th} and the associated increase in the filling of the energy bands.

By characterizing additional laser structures with asymmetric bounding layers, we found that the upper bounding layer was essential, while the lower bounding layer had only a very small effect. Auger electron spectroscopy and photoluminescence measurements on test wafers revealed that the upper bounding layer was effective in suppressing the diffusion of In out from the InGaAs layer during the heating period when the substrate temperature was raised from 640 to 800°C.

The optimum thickness of the bounding layer depends on the InAs mole fraction in the active layer. As will be discussed later, for lasers with smaller x, thinner bounding layers are preferable because carrier leakage from the active layer to the bounding layers decreases with decreasing t. For smaller values of x, thinner bounding layers are sufficient to suppress In out-diffusion.

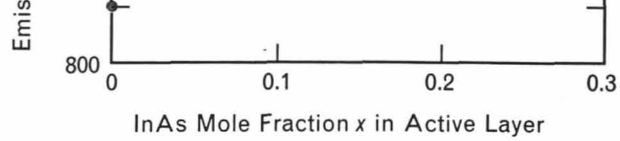

FIGURE 3. Laser emission wavelength as a function of x in the $In_xGa_{1-x}As$ active layer for a cavity length L = 500 μm.

Effect of InAs mole fraction. Broad-stripe lasers were fabricated from wafers with x ranging from 0 to 0.3. To increase the optical confinement and hence reduce J_{th}, the value of y in the confining layers was graded from 0.08 to 0.7, except for three wafers in which x = 0, 0.02, and 0.05. For these three wafers, y was graded between 0.2 and 0.7, and t was varied from 0 to 1.5 nm. For one wafer with x = 0.05, t was 5 nm, and for all the other wafers, t was 10 nm.

We found that the laser characteristic most affected by a change in x was the emission wavelength. Figure 3 plots the emission wavelength versus x for L = 500 μm. As x increases from 0 to 0.3, the emission wavelength increases from 850 to 1060 nm. The measured wavelengths are in good agreement with theoretical values (the solid line in Figure 3) calculated [5] by taking into account three factors: (1) the bulk bandgap energy of InGaAs alloys, (2) the increase in bandgap energy due to compressive strain, and (3) the increase in the electron-hole transition energy due to the quantization of the energy levels in the quantum well. Because of the limitation imposed by the critical thickness discussed earlier, the longest wavelength that InGaAs/AlGaAs lasers can attain is ~1100 nm. Lasers with layers in which y was graded from 0.2 to 0.7 (denoted as 0.2–0.7 GRIN) had somewhat shorter emission wavelengths than the theoretical values because the quantized level was higher than expected. For x = 0.05, the emission wavelength was 882 nm with 0.2–0.7 GRIN layers, compared to 895 nm with 0.08–0.7 GRIN layers.

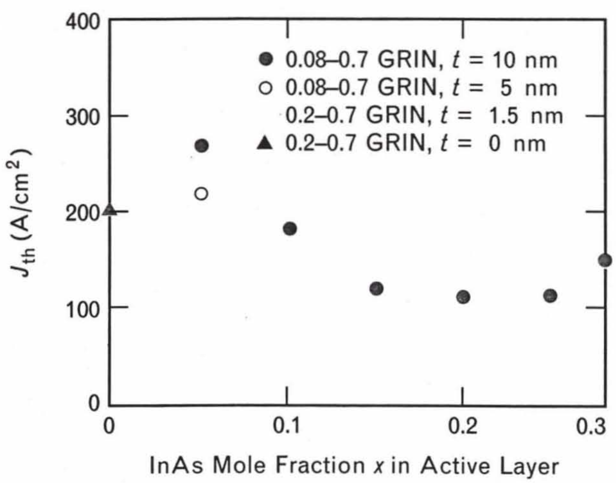

FIGURE 4. Threshold current density J_{th} as a function of x in the active layer.

Figure 4 shows the dependence of J_{th} on x. For devices with t = 10 nm and 0.08–0.7 GRIN layers, the value of J_{th} is nearly constant at 110 to 120 A/cm^2 for $0.15 \leq x \leq 0.25$. These values are much smaller than the 200 A/cm^2 obtained for GaAs/AlGaAs lasers with 0.2–0.7 GRIN layers. The reduction in J_{th} in InGaAs/AlGaAs lasers had been predicted [18, 19] because the compressive strain reduces the density of states—i.e., the number of allowed electronic states per unit energy—in the valence band of InGaAs (see the box, "The Concept of Strained Layers"). The effect of the difference in the GRIN layers is minor: for x = 0.25 the change from 0.08–0.7 to 0.2–0.7 GRIN layers increases J_{th} from 114 to only 125 A/cm^2.

For $x \leq 0.1$ and t = 10 nm, the value of J_{th} increases because the strain is reduced and the shallower well depth increases the leakage current from the quantum well to the bounding layers. For x = 0.05, the value of J_{th} is equal to 263 A/cm^2. We reduced the leakage current by decreasing t and increasing the minimum value of y. By decreasing t to 5 nm, we reduced the value of J_{th} to 216 A/cm^2. The value of J_{th} was further reduced to 186 A/cm^2 by a decrease in t to 1.5 nm coupled with the use of 0.2–0.7 GRIN layers.

For x = 0.3 and t = 10 nm, the value of J_{th} is 140 A/cm^2, a slight increase from the J_{th} values for the range $0.15 \leq x \leq 0.25$. The increase might result from an unoptimized value of t or some nonradiative recombination mechanism that increases with x.

Figure 5 shows the dependence of η_d on x. The value

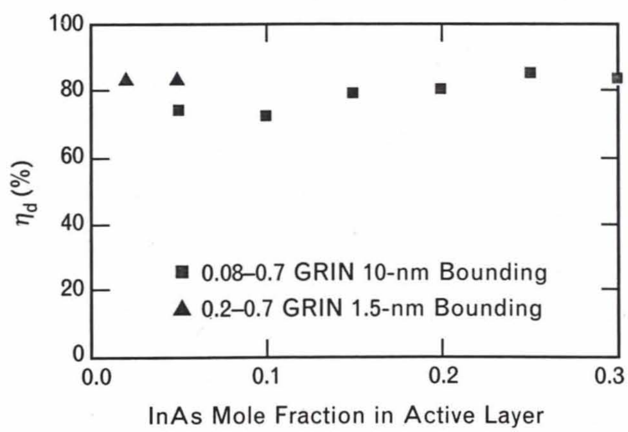

FIGURE 5. Differential quantum efficiency η_d as a function of x for lasers with L = 500 μm.

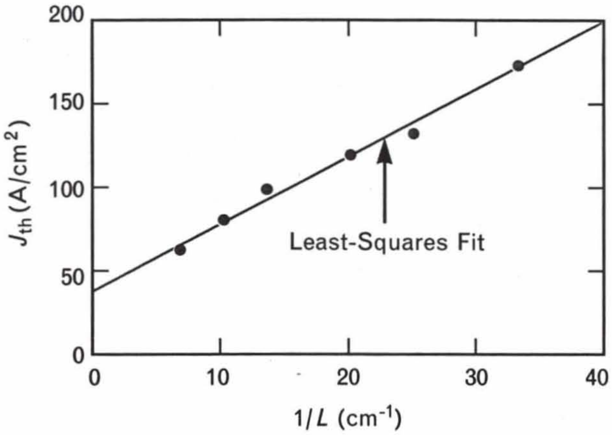

FIGURE 6. Dependence of threshold current density J_{th} on reciprocal cavity length $1/L$ for $In_{0.25}Ga_{0.75}As$/AlGaAs diode lasers.

of η_d is between 80 and 85% for $x > 0.15$. For $x < 0.1$ and $t = 10$ nm, the value of η_d decreases to between 72 and 76% because of the increase in leakage current to the bounding layers. Reducing the leakage current increases the value of η_d. For lasers with $x = 0.05$, $t = 1.5$ nm, and 0.2–0.7 GRIN layers, the value of η_d is 83%.

Effect of cavity length. We measured the P-I characteristics of lasers with $x = 0.25$ for L values ranging from 300 to 1500 μm. Figure 6 shows J_{th} as a function of $1/L$. As L increases, the value of J_{th} decreases monotonically because the output coupling loss normalized to L decreases. For $L = 1500$ μm ($1/L = 6.7$ cm^{-1}), the value of J_{th} is equal to 65 A/cm^2—the lowest value obtained for any InGaAs/AlGaAs laser.

Figure 7 is a plot of η_d^{-1} versus L. The value of η_d for $L = 300$ μm is 90%—the highest value obtained for InGaAs/AlGaAs lasers. Because of photon loss inside the cavity, the value of η_d decreases monotonically as L is increased. From Figure 7, we can deduce the internal quantum efficiency η_i and the internal loss coefficient α_i for photons. The parameter η_i is defined as the number of emitted photons per injected electron above threshold. The value depends on the efficiency of carrier collection to the active layer and the ratio of radiative to nonradiative recombination. The parameter α_i measures how strongly photons are absorbed or scattered as they propagate along the waveguide. In most lasers, the loss is dominated by free-carrier absorption. A smaller value of α_i is desirable because the value of η_d is less sensitive to L for small α_i. Since the thermal resistance is inversely proportional to L, a higher output power is expected from lasers with a lower value of α_i. The relationship between η_d, η_i, and α_i above threshold is

$$\eta_d^{-1} = \eta_i^{-1}\left[\frac{\alpha_i L}{\ln(1/R)} + 1\right],$$

where R is the facet reflectivity. From Figure 7, the value of η_i is approximately 100% (obtained from the y-intercept) and the value of α_i is approximately 5 cm^{-1} (obtained from the slope). By reducing the carrier density near the active region, we have obtained values of α_i as small as 1.5 cm^{-1} in other laser structures.

From Figure 6, we can deduce the gain coefficient β, which measures the rate with which the optical gain increases as the current is increased, and the transparency current density J_{tr}, which is the value at which the active layer neither absorbs nor amplifies the light at the lasing wavelength. Both of these quantities are related to the density of states. Because the density of states is smaller for compressively strained InGaAs than for GaAs, a lower value of J_{tr} and a higher value of β are expected. The relationship between J_{th}, J_{tr}, and β is given by

$$J_{th} = \frac{1}{\eta_i}\left[J_{tr} + \frac{d}{\beta\Gamma}\left(\alpha_i + \frac{\ln(1/R)}{L}\right)\right], \quad (1)$$

where Γ is the confinement factor, which is defined as the fraction of light in the active layer. From the slope of the curve in Figure 6, we calculate the value of β to be 0.085 cm μm A^{-1}, about 60% higher than the value obtained for GaAs/AlGaAs quantum-well lasers. Using Equation 1 along with the y-intercept and the values $\alpha_i = 5$ cm^{-1} and $\Gamma = 0.025$, we obtain $J_{tr} = 25$ A/cm^2—

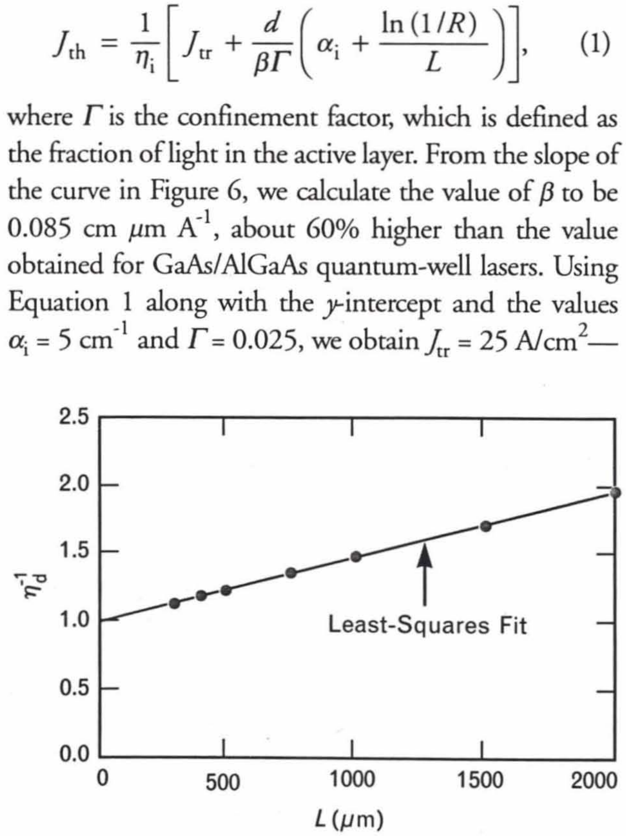

FIGURE 7. Dependence of reciprocal differential quantum efficiency η_d^{-1} on cavity length L for $In_{0.25}Ga_{0.75}As$/AlGaAs diode lasers.

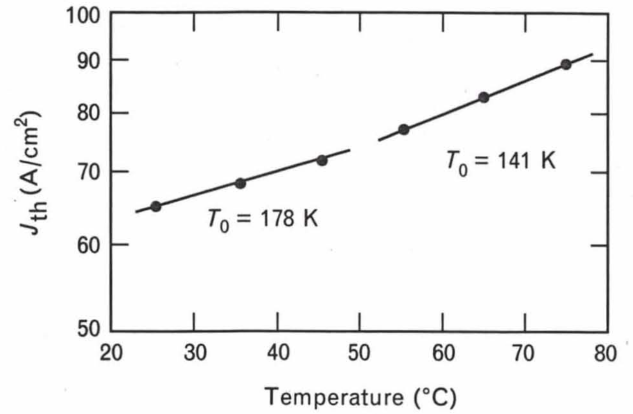

FIGURE 8. Dependence of threshold current density J_{th} on temperature for $In_{0.25}Ga_{0.75}As$/AlGaAs diode laser 300 μm wide × 1500 μm long.

the lowest value reported for any semiconductor laser.

Effect of temperature on J_{th}. The value of J_{th} increases with temperature because of a decrease in gain and an increase in leakage current as well as the effects of nonradiative recombination. Figure 8 shows the temperature dependence of J_{th} for 1500-μm-long devices with $x = 0.25$. The value of J_{th} increases from 65 A/cm^2 at 25°C to 90 A/cm^2 at 75°C. The temperature dependence of J_{th} is typically described by the characteristic temperature T_0 that appears in the expression $J_{th}(T) = J_0[\exp(T/T_0)]$, where T is the absolute temperature and J_0 is an empirical parameter. Higher values of T_0 are preferable because they imply that J_{th} is less sensitive to temperature. The value of T_0 for the device shown in Figure 8 is 178 K between 25° and 45°C and 141 K between 55° and 75°C. The value of T_0 in the lower temperature range decreases with decreasing cavity length to 159 K for L = 1000 μm, and 137 K for L = 300 μm. These values are comparable to those obtained for GaAs/AlGaAs quantum-well lasers.

Continuous-Wave Operation

For continuous-wave (CW) operation, several devices with $x = 0.25$ were mounted junction side down on copper heat sinks with In solder. A thermopile detector measured the output power. Figure 9 shows the P-I curve for an uncoated laser with L = 1000 μm and width W = 300 μm. The threshold current is about 240 mA, and η_d is about 62%. The maximum output power from both facets is limited to 3.2 W by the junction-temperature rise. Figure 9 also shows the power conversion efficiency, the total optical power divided by the electrical power input. The power efficiency is always smaller than η_d because of the finite values for threshold current and series resistance. With a series resistance of about 0.07 Ω, the maximum power efficiency is about 47%. The power efficiency decreases at higher currents because the junction-temperature rise reduces η_d.

Reliability

In view of the high strain levels in the active layer, the reliability of InGaAs/AlGaAs lasers has often been questioned. Several experiments, however, indicate that these lasers will prove to exhibit greater reliability than the more mature GaAs/AlGaAs lasers [11, 20, 21]. A dramatic demonstration of the comparative reliability of InGaAs/AlGaAs and GaAs/AlGaAs lasers has been reported by R.G. Waters et al. [21]. To accelerate degradation, damage was introduced by scribing a line next to the active stripe. The GaAs/AlGaAs lasers degraded rapidly by the propagation of dark-line defects, the dislocation networks that are the most common cause of sudden degradation in such lasers. On the other hand, InGaAs/AlGaAs lasers showed stable operation because the formation of dark-line defects was greatly reduced. The most plausible explanation for the greater reliability of InGaAs/AlGaAs lasers is lattice hardening that results because In atoms are significantly larger than

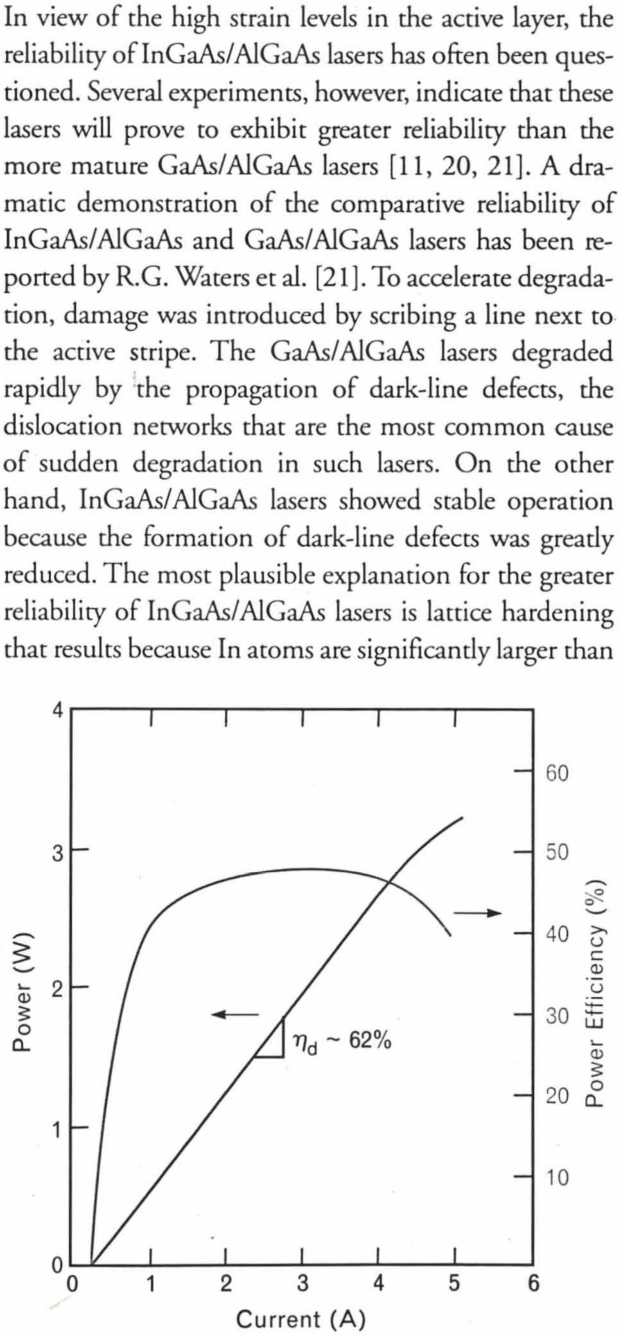

FIGURE 9. CW output power and power conversion efficiency versus current for an InGaAs/AlGaAs laser 300 μm wide × 1000 μm long.

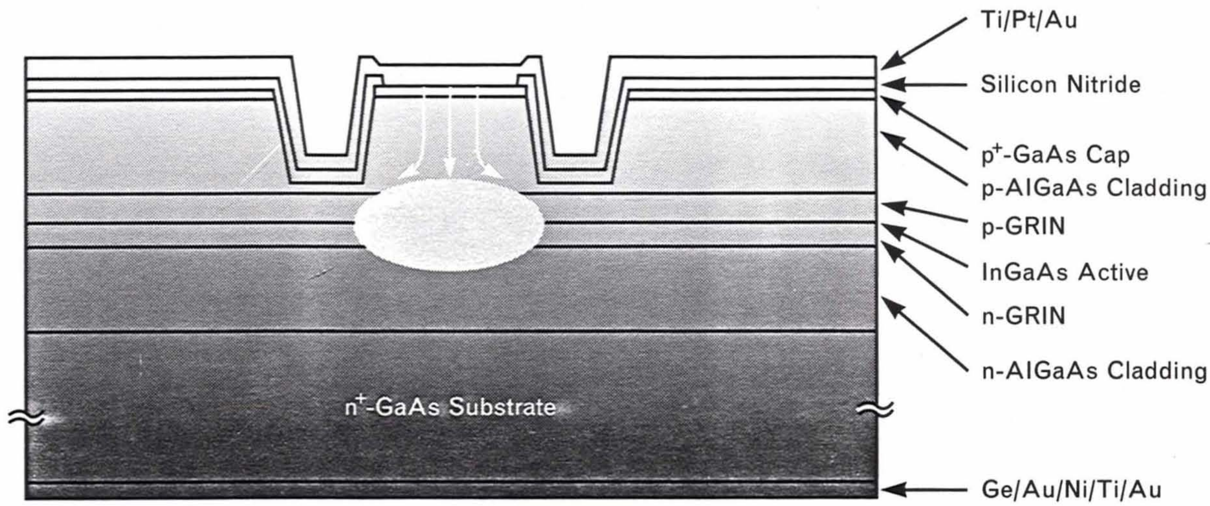

FIGURE 10. Schematic diagram of the structure of a ridge-waveguide laser.

Ga, Al, and As atoms, all of which are nearly the same size [22]. However, InGaAs/AlGaAs lasers with an active layer thicker than the critical thickness degrade very rapidly because dislocations are formed to accommodate the lattice mismatch with the confining layers.

Narrow-Stripe Lasers

For many applications, lasers with low threshold currents are desirable. Confining both the current and optical field of a laser reduces the threshold current. For a tight optical mode, the waveguide must have a sufficiently large refractive-index step Δn in the direction parallel to the epilayer. If Δn is too large, however, multiple modes can be supported, and the optical field can switch to a higher-order mode as the power is increased. For the mode to be stable over a wide power range, the waveguide should support only a single mode. The optimum Δn increases with decreasing stripe width. For 3-μm-wide stripes, the optimum Δn is approximately 5×10^{-3}.

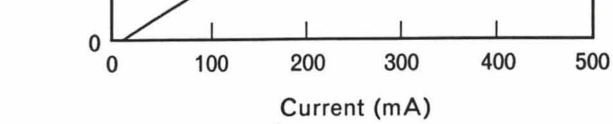

FIGURE 11. Output power versus current for InGaAs/AlGaAs ridge-waveguide laser.

We selected a ridge-waveguide structure (Figure 10) for index-guided lasers because this structure is relatively simple to fabricate. In ridge waveguides, the value of Δn is determined by the difference in the thicknesses of the p-AlGaAs cladding layer in the etched and unetched regions. The depth of etching is thus crucial for obtaining the appropriate Δn for a single-mode waveguide.

To etch the ridge, we used reactive ion etching in a plasma formed by a mixture of BCl_3 and Ar gases. This process etches GaAs and AlGaAs at the same rate, and it produces very little undercutting beneath the photoresist. The insulating silicon-nitride layer, which covers the entire surface except the mesa center, confines the current. A Ti/Pt/Au metallization was used to make ohmic contacts to the p^+-GaAs layer.

Figure 11 shows the P-I characteristic of a pulsed ridge-waveguide laser with $x = 0.15$ and uncoated facets. The threshold current is about 8 mA and η_d is 80%. The maximum power from both facets is more than 400 mW. The far-field pattern parallel to the junction is shown in Figure 12 at six current levels in 50-mA steps. The figure shows a fundamental Gaussian mode with a full width at half maximum (FWHM) of ~23° up to 200 mA. At 250 mA, the far-field pattern becomes slightly asymmetric, indicating that the first-order mode has begun to lase. At 300 mA, the asymmetry is more apparent.

We have operated ridge-waveguide lasers with un-

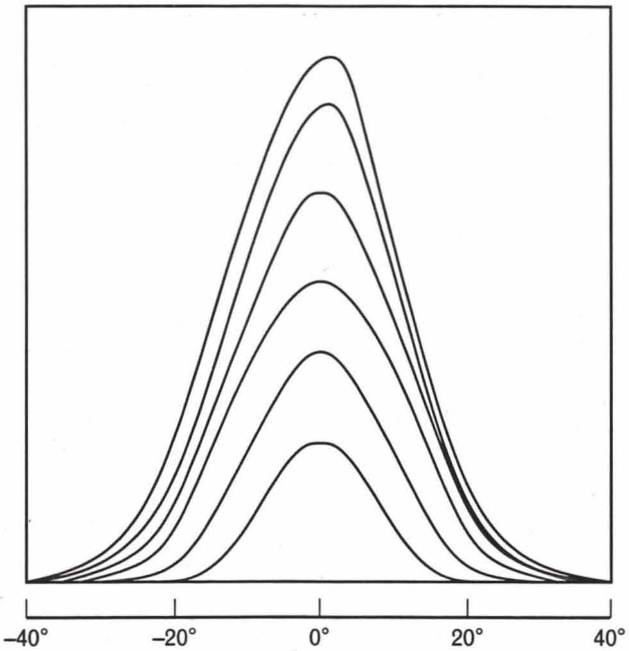

FIGURE 12. Far-field pattern of InGaAs/AlGaAs ridge-waveguide laser at six different current levels in 50-mA steps, from 50 mA to 300 mA.

coated facets in CW mode up to a level of 30 mW per facet. The output power was limited by the temperature rise that resulted from heating due to the series resistance.

GaInAsSb/AlGaAsSb Double-Heterostructure Lasers

Figure 13 shows the bandgap energy versus lattice constant for GaInAsSb and AlGaAsSb alloys at room temperature. Lines that connect the binary compounds represent ternary alloys, and the shaded regions bounded by the lines represent quaternary alloys. The compositions of $Ga_{1-x}In_xAs_ySb_{1-y}$ alloys that are lattice matched to GaSb satisfy the following relationship:

$$y = \frac{0.91(1-x)}{1+0.05x}.$$

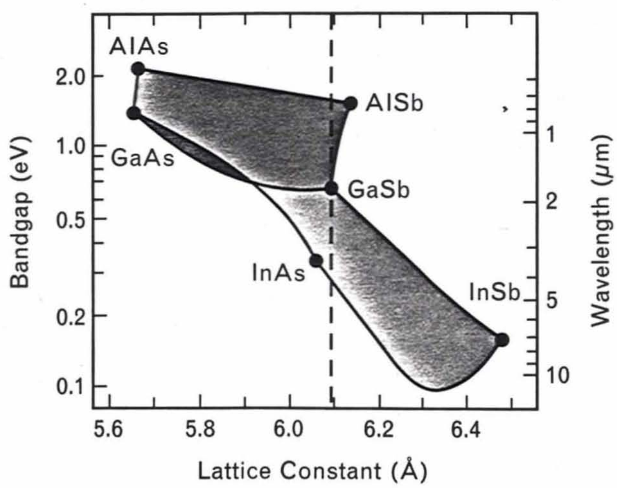

FIGURE 13. Bandgap energy versus lattice constant for GaInAsSb and AlGaAsSb at 300 K.

In Figure 14, the room-temperature values of the bandgap energy E_g and corresponding wavelength λ_g of the lattice-matched alloys are plotted versus x. Note that E_g is almost constant for $x < 0.4$ and has a minimum of 0.28 eV ($\lambda_g = 4.4\ \mu m$) at $x = 0.22$.

We chose AlGaAsSb for the laser cladding layers because, unlike GaSb, it has a lower refractive index than GaInAsSb and provides potential barriers high enough to confine both electrons and holes to the GaInAsSb layer. Since AlSb and GaSb have a lattice mismatch of ~6.5×10^{-3} (about five times larger than that between AlAs and GaAs), a small amount of As needs to be incorporated to avoid misfit dislocations.

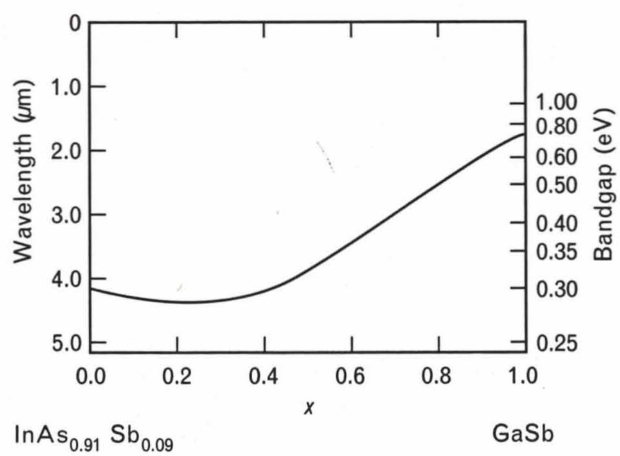

FIGURE 14. Bandgap emission wavelength and energy at 300 K versus x for $Ga_xIn_{1-x}As_ySb_{1-y}$ lattice matched to GaSb, with $y = 0.91(1-x)/(1+0.05x)$.

The first GaInAsSb/AlGaAsSb diode lasers were reported by N. Kobayashi et al. [23] in 1980. These devices, which used a $Ga_{0.95}In_{0.05}As_{0.04}Sb_{0.96}$ active layer and $Al_{0.2}Ga_{0.8}As_{0.02}Sb_{0.98}$ cladding layers, operated at room temperature with an emission wavelength of 1.8 μm and J_{th} as low as 5 kA/cm^2. Since then, improving the quality of the epilayers and increasing the Al content of the cladding layers have gradually reduced the value of J_{th} [24–31]. The lowest reported value for

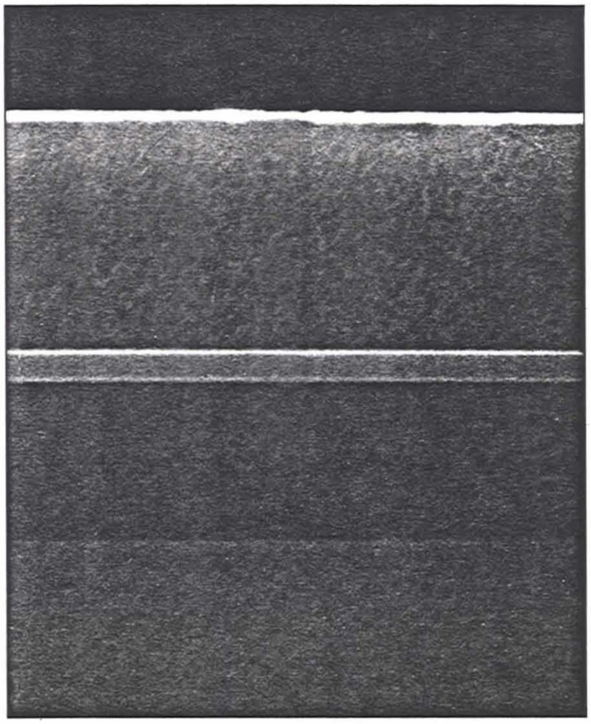

FIGURE 15. Scanning electron micrograph of GaInAsSb/AlGaAsSb laser structure.

J_{th} is 1.5 kA/cm^2, which was obtained for lasers that used $Al_xGa_{1-x}As_ySb_{1-y}$ layers with $x = 0.55$ [27]. Room-temperature CW operation has been achieved by two groups [27, 28]. One of the groups, A.E. Bochkarev et al. [27], obtained threshold currents as low as 80 mA for ridge-waveguide lasers with an emission wavelength of 2.34 μm.

Epitaxy of GaInAsSb/AlGaAsSb Laser Structure

Most of the previously reported GaInAsSb/AlGaAsSb lasers have been grown by liquid phase epitaxy (LPE). Although high-quality material can be grown by LPE, this technique has several limitations. First, there is a miscibility gap in the $Ga_{1-x}In_xAs_ySb_{1-y}$ system for compositions with bandgaps that correspond to a wavelength region between 2.4 and 4 μm [32]. Second, growth of lattice-matched AlGaAsSb layers becomes more difficult with increasing Al content because incorporation of sufficient As for lattice matching requires the growth temperature to be increased significantly [33]. Finally, because LPE does not provide good thickness control or uniformity, the technique is not well suited for fabricating quantum-well structures for higher-performance lasers.

Molecular-beam epitaxy (MBE), which does not have such drawbacks, has also been used to grow GaInAsSb/AlGaAsSb lasers [24, 31]. Before we started our research effort in late 1988, lasers grown by MBE had characteristics considerably inferior to lasers grown by LPE. The lowest threshold current density achieved at room temperature was 4.2 kA/cm^2 [24]. Our MBE-grown lasers have much improved characteristics, with J_{th} as low as 1.5 kA/cm^2 (equal to the lowest value reported [27] for GaInAsSb/AlGaAsSb devices), η_d as high as 50%, and pulsed output power as high as 1.8 W from both facets.

In MBE, epilayers are deposited on a heated substrate by the simultaneous evaporation of several beams of molecules in an ultrahigh vacuum [34]. The beam fluxes are individually controlled by adjusting the temperatures of the crucibles holding the different sources.

The sources we used for growing GaInAsSb and AlGaAsSb were the Group III and Group V elements, which yielded beams of Al, Ga, and In atoms, and As_4 and Sb_4 molecules. The n-type dopant was Te, which was provided by the sublimation of GaTe, and the p-type dopant was Be. As in the MBE growth of other III-V semiconductors, during epilayer deposition the total Group V flux was greater than the total Group III flux.

Lattice-matching the alloys to the substrate required very careful adjustment of each beam flux. Because the total thickness of the AlGaAsSb cladding layers was ~5 μm, the lattice mismatch $\Delta a/a_{sub}$ would have to be less than 10^{-3} to avoid dislocation formation. (Note: $\Delta a = a_{epi} - a_{sub}$, where a_{epi} and a_{sub} are the lattice constants of the epilayer and substrate, respectively.) Because of its smaller thickness, the GaInAsSb active layer could tolerate a slightly larger lattice mismatch. Adjusting the fluxes of Al, Ga, and In was straightforward because their incorporation efficiency is equal to unity. Therefore, the ratio of these elements in an alloy epilayer is just equal to the ratio of their fluxes. Selecting the proper fluxes for Sb and As was more difficult, however, because Sb is incorporated much more readily than As. Consequently, we controlled the As and Sb mole fractions in GaInAsSb and AlGaAsSb by using a large excess As flux and reducing the ratio of Sb to the total Group III elements far enough below 1 to yield the desired composition.

The optimization of the growth conditions required a number of iterations. First, a test layer was characterized by X-ray diffraction to check the lattice mismatch, by Auger electron spectroscopy to examine the composition, and by infrared absorption to measure the approximate bandgap. Using this information, we adjusted the beam fluxes to obtain better lattice matching. When the lattice matching was acceptable, the layer was further characterized by low-temperature photoluminescence to check the optical quality and to obtain a more precise bandgap measurement. We repeated these steps until satisfactory growth conditions were established.

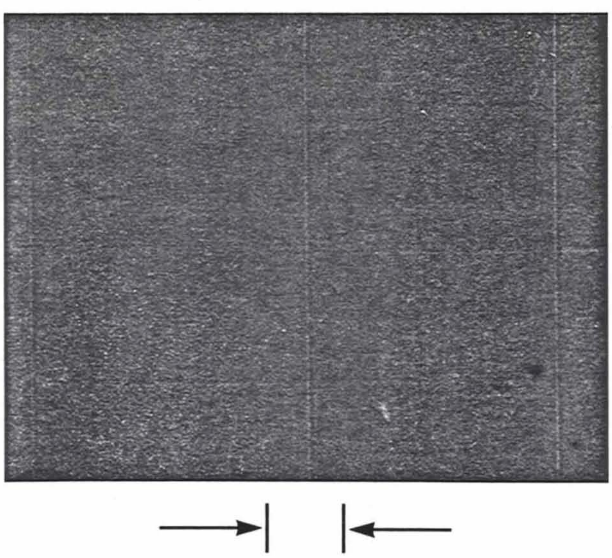

FIGURE 16. Nomarski photomicrograph showing surface morphology of GaInAsSb/AlGaAsSb laser structure.

The laser structures were grown on commercial Te-doped GaSb substrates. Figure 15 is a scanning electron micrograph that shows a cross section of a GaInAsSb/AlGaAsSb laser structure. From bottom to top, the structure consists of a 0.2-μm-thick n$^+$-GaSb buffer layer, a 2-μm-thick n-$Al_{0.5}Ga_{0.5}As_{0.04}Sb_{0.96}$ cladding layer, a 0.4-μm-thick nominally undoped $Ga_{0.84}In_{0.16}As_{0.14}Sb_{0.86}$ active layer, a 3-μm-thick p-$Al_{0.5}Ga_{0.5}As_{0.04}Sb_{0.96}$ cladding layer, and an 0.05-μm-thick p$^+$-GaSb cap layer.

We selected the composition of the active layer for lasing at 2.3 μm. The carrier concentrations in the n- and p-AlGaAsSb cladding layers were about 1×10^{17} and 6×10^{16} cm^{-3}, respectively. The doping concentration of the p$^+$-GaSb cap layer was 2×10^{18} cm^{-3}.

Figure 16 shows that the surface morphology of the laser structure was very smooth. Note, however, the cross-hatch pattern in the photomicrograph. The pattern is a result of a slight residual lattice mismatch. From a double-crystal X-ray diffraction measurement, we find the mismatch to be about 1.5×10^{-3}.

Laser Characteristics

We fabricated 300-μm-wide broad-stripe lasers by a process similar to the one used to fabricate InGaAs/AlGaAs lasers. The p$^+$- and n-GaSb layers were metallized with Ti/Au and Au/Sn/Au, respectively, and the alloying was performed at 300°C in a H_2 atmosphere. (In a separate study of test samples, we measured specific contact resistances of less than 5×10^{-5} Ω-cm^2 for both the p and n contacts.) Next, the wafer was cleaved into bars with a cavity length L that ranged from 300 to 700 μm. Using In, we then mounted the bars junction side up on copper heat sinks.

Figure 17 shows the current versus voltage characteristic of a 300×300-μm GaInAsSb/AlGaAsSb laser. The turn-on voltage is about 0.25 V and the series resistance is about 1.5 Ω. In the reverse direction, the leakage current is about 250 and 500 μA at −1 and −2 V, respectively. The leakage current is sensitive to the amount of lattice mismatch and the quality of the epilayer material. In general, lasers with larger leakage currents have poorer lasing characteristics.

We probe-tested the lasers under pulsed condition at room temperature. Figure 18 shows the emission spectrum of a laser 300 μm long at approximately 1.15 times the threshold current. The output shows multiple longitudinal modes, as is typically observed in broad-stripe lasers. The peak wavelength is located at 2.275 μm, which is very close to the design wavelength of 2.3 μm. From the mode spacing of about 23 Å, we find the group refractive index n^* to be about 3.71. The group refractive index is defined by

$$n^* \equiv n\left[1 - \frac{\lambda}{n}\left(\frac{dn}{d\lambda}\right)\right],$$

where n is the effective refractive index of the double heterostructure, and λ is the wavelength.

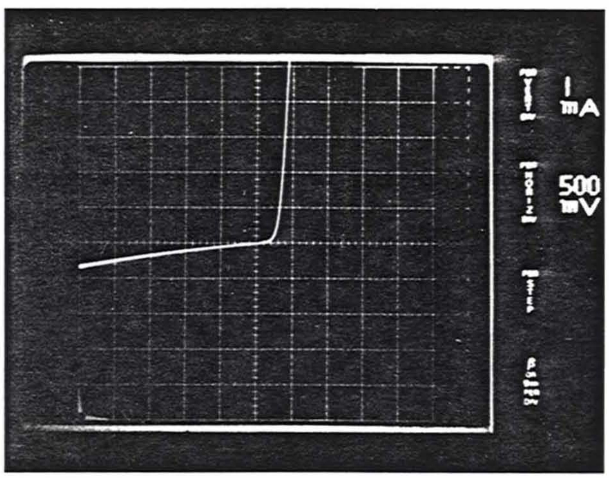

FIGURE 17. Voltage versus current for GaInAsSb/AlGaAsSb laser.

Measuring the pulsed output power of the lasers is not a straightforward task because no large-area photodetector with high sensitivity and high speed is available for wavelengths beyond 2 μm. We selected a pyroelectric detector because of its relatively low minimum detectable signal, wide dynamic range, and flat spectral response. Because of the low detector responsivity, however, the RF pickup noise was larger than the photosignal when the laser was placed close enough to the detector to avoid the use of collecting optics. Since the laser has a large beam divergence, we used an ellipsoidal reflector to collect most of the light. The laser was located at one focal point of the ellipse and the pyroelectric detector

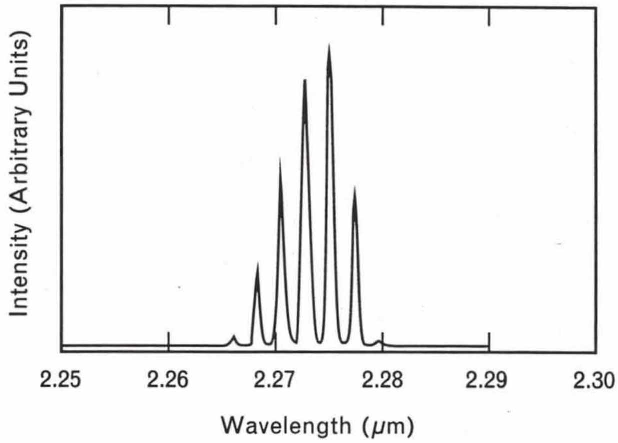

FIGURE 18. Emission spectrum of GaInAsSb/AlGaAsSb diode laser for pulsed operation at room temperature.

was located at the other. We obtained the output power by dividing the average energy measured per pulse by the pulse width, which was generally 500 nsec.

Figure 19 shows the dependence of J_{th} on L. As L increases from 300 to 700 μm, J_{th} decreases monotonically from 1.8 to 1.5 kA/cm^2, which is equal to the lowest reported value for GaInAsSb/AlGaAsSb lasers [27]. These values are considerably lower than the one calculated by A. Sugimura [35], who assumed that Auger recombination is the main nonradiative loss mechanism. In addition, J_{th} did not show any significant dependence on wavelength in the region from 1.8 to 2.3 μm [26]. These results indicate that Auger recombination is not the dominant loss mechanism in this wavelength region.

Figure 20 is a plot of η_d^{-1} versus L. The value of η_d decreases from 47% for L = 300 μm to 27% for

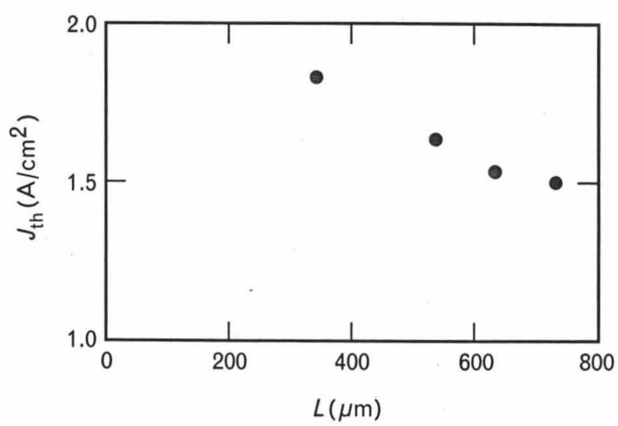

FIGURE 19. Dependence of threshold current density J_{th} on cavity length L.

L = 700 μm. From the slope of the straight line drawn through the data points and the assumption that R = 0.3, we calculate the internal loss coefficient α_i to be ~43 cm^{-1}, which is comparable to values obtained for InGaAsP/InP double-heterostructure lasers [36]. The internal quantum efficiency obtained from the y-intercept is ~100%.

Figure 21 shows the P-I characteristic of a 300 × 300-μm device. We reduced the pulse width to 200 nsec in order to decrease the temperature rise at the junction and to increase the current level that could be used without damaging the device at the point contact to the Ti/Au metallization. The value of η_d is ~50%, and the maximum power from both facets is 1.8 W, which was

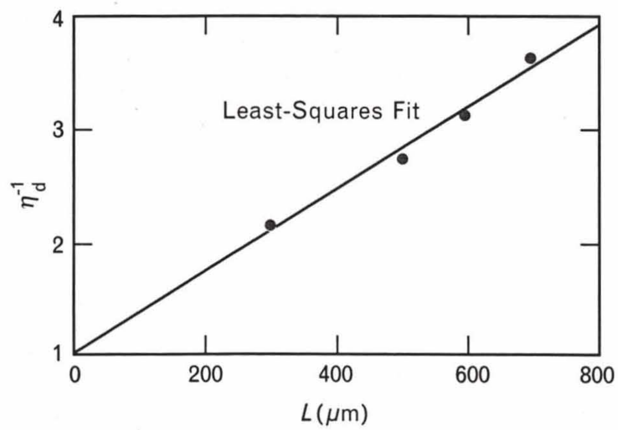

FIGURE 20. Dependence of reciprocal differential quantum efficiency η_d^{-1} on cavity length L.

obtained at 9 A. (The output power was limited by the failure of the point contact.) These are the highest room-temperature values obtained for any semiconductor laser emitting beyond 2 μm.

We measured P-I curves for another 300 × 300-μm laser at temperatures from –120 to 20°C. Figure 22, which plots J_{th} as a function of temperature, shows that J_{th} = 190 A/cm^2 at –120°C. The characteristic temperature T_0 is ~75 K and 50 K near –120°C and 20°C, respectively. These values are comparable to the best values that have been reported for GaInAsSb/AlGaAsSb lasers [25, 27, 29]. The decrease of T_0 with increasing temperature may indicate that Auger recombination becomes more important at higher temperatures.

Figure 23 shows the near-field pattern recorded with a PbS camera for a 300 × 300-μm device. Except for some filamentation that commonly exists in broad-stripe la-

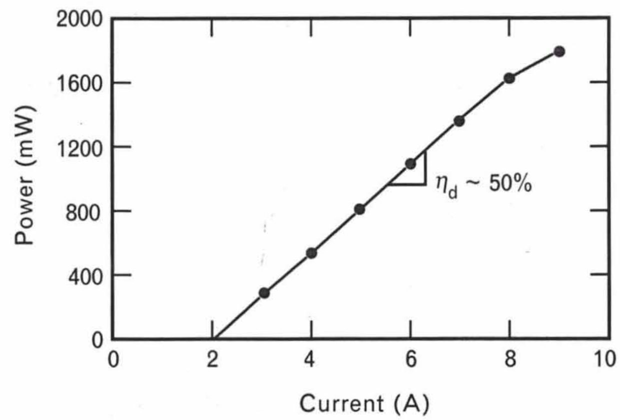

FIGURE 21. Light output versus current for GaInAsSb/AlGaAsSb laser 300 μm wide by 300 μm long. The data are for pulsed operation at 295 K.

sers, the pattern is fairly uniform, which indicates good spatial uniformity of the epilayers. The far-field pattern in the direction normal to the junction is shown in Figure 24. The FWHM is ~65°. The large divergence angle indicates a fairly tight confinement of the mode to the active layer, since this angle is inversely proportional to the beam size. The refractive index step, calculated by using an approximate expression relating this step to the divergence [37], is ~0.35. The refractive indexes of GaInAsSb and AlGaAsSb have not been measured.

Conclusion

Although relatively new, InGaAs/AlGaAs strained-layer quantum-well lasers have already demonstrated state-of-the-art performance. Their rapid progress has been possible because the technology that has been developed for the growth and fabrication of GaAs/AlGaAs lasers is directly applicable. With the benefit of enhanced reli-

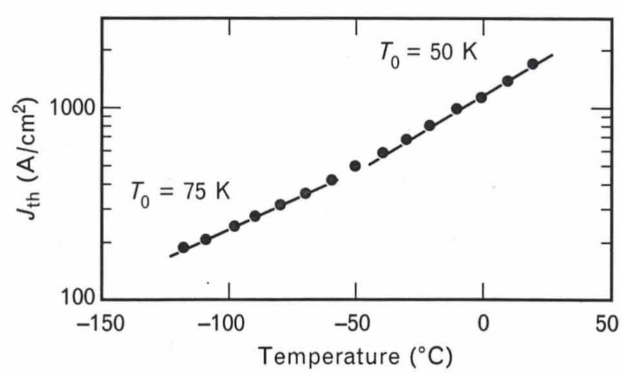

FIGURE 22. Dependence of threshold current density J_{th} on temperature for GaInAsSb/AlGaAsSb laser 300 μm wide × 300 μm long.

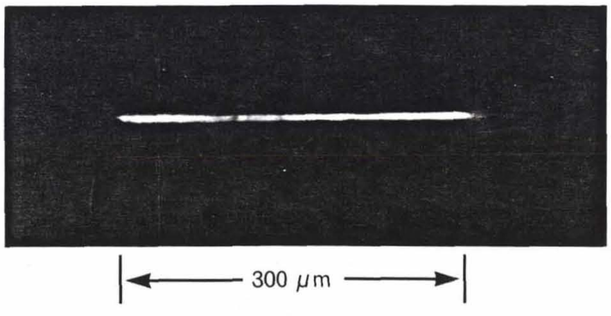

FIGURE 23. Near-field pattern of GaInAsSb/AlGaAsSb laser measured by PbS camera.

ability that results from the addition of In, InGaAs/AlGaAs lasers will be extremely useful for applications requiring emission wavelengths in the range from 0.9 to 1.1 μm.

While GaInAsSb/AlGaAsSb lasers are still in an early stage of development, the results already obtained are much better than had been anticipated. With many applications awaiting lasers that emit at 2 to 4 μm, the field is wide open for much work. Areas that call for further effort include optimization of the epilayer growth parameters, development of index-guided structures for low threshold currents, development of quantum-well structures for improved performance, and extension of the emission wavelength to 4 μm, as well as additional theoretical study of the material system and measurement of basic parameters such as the refractive index.

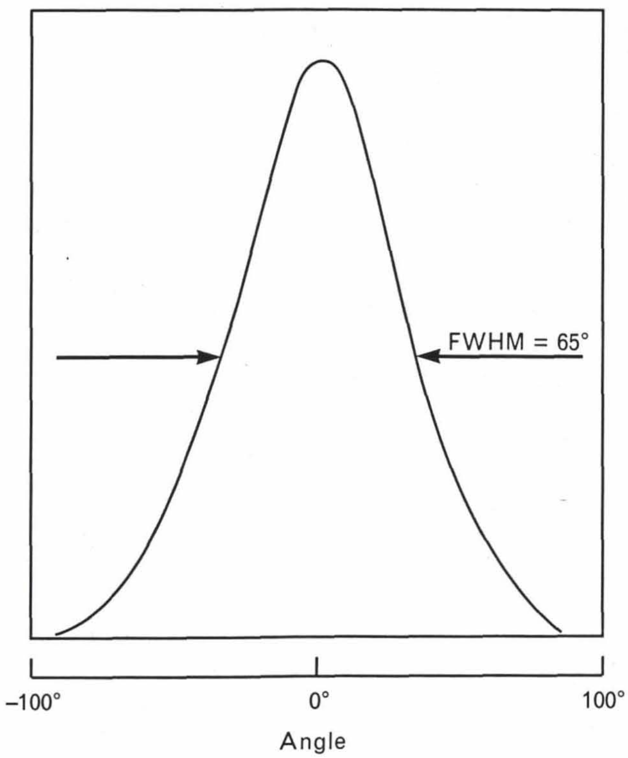

FIGURE 24. Far-field pattern of GaInAsSb/AlGaAsSb laser in the direction normal to the junction.

Acknowledgments

The authors are grateful for the expert technical assistance of M.K. Connors, B. DiGiorgio, W.L. McGilvary, and G.D. Silva in laser fabrication; and of D.F. Kolesar and B.A. Nechay in establishing the laser-measurement setup. The authors also acknowledge the contributions of G.W. Turner and J.W. Chludzinski for photoluminescence and laser emission spectroscopy; P.M. Nitishin for scanning electron microscopy; and J.V. Pantano and D.M. Tracy for epitaxial growth. The continued interest and helpful suggestions of A.J. Strauss and I. Melngailis are gratefully appreciated.

This work was sponsored by the Department of the Air Force.

REFERENCES

1. C.A. Wang, "A New Organometallic Vapor Phase Epitaxy Reactor for Highly Uniform Epitaxy," *Lincoln Laboratory J.* **3**, 3 (1990).
2. P. Lacovara, H.K. Choi, C.A. Wang, R.L. Aggarwal, and T.Y. Fan, "Diode-Pumped Room Temperature Yb:YAG Laser," submitted to *Optics Lett.*
3. M. Yamada, M. Shimizu, T. Takeshita, M. Okayasu, M. Horiguchi, S. Uehara, and E. Sugita, "Er^{3+}-Doped Fiber Amplifier Pumped by 0.98 μm Laser Diodes," *IEEE Photon. Technol. Lett.* **1**, 422 (1989).
4. D.C. Tran, G.H. Sigel, Jr., and B. Bendow, "Heavy Metal Fluoride Glasses and Fibers: A Review," *J. Lightwave Technol.* **LT-2**, 566 (1984).
5. R.M. Kolbas, N.G. Anderson, W.D. Laidig, Y. Sin, Y.C. Lo, K.Y. Hsieh, and Y.J. Yang, "Strained-Layer InGaAs-GaAs-AlGaAs Photopumped and Current Injection Lasers," *IEEE J. Quant. Electron.* **24**, 1605 (1988).
6. W.T. Tsang, "Extension of Lasing Wavelengths beyond 0.87 μm in GaAs/$Al_xGa_{1-x}As$ Double-Heterostructure Lasers by In Incorporation in the GaAs Active Layers during Molecular Beam Epitaxy," *Appl. Phys. Lett.* **38**, 661 (1981).
7. M.D. Camras, J.M. Brown, N. Holonyak, Jr., M.A. Nixon, R.W. Kaliski, M.J. Ludowise, W.T. Dietze, and C.R. Lewis, "Stimulated Emission in Strained-Layer Quantum-Well Heterostructures," *J. Appl. Phys.* **54**, 6183 (1983).
8. W.D. Laidig, P.J. Caldwell, Y.F. Lin, and C.K. Peng, "Strained-Layer Quantum-Well Injection Laser," *Appl. Phys. Lett.* **44**, 653 (1984).
9. D. Feketa, K.T. Chan, J.M. Ballantyne, and L.F. Eastman, "Graded-Index Separate-Confinement InGaAs/AlGaAs Strained-Layer Quantum Well Laser Grown by Metalorganic

Chemical Vapor Deposition," *Appl. Phys. Lett.* 49, 1659 (1986).
10. W. Stutius, P. Gavrilovic, J.E. Williams, K. Meehan, and J.H. Zarrabi, "Continuous Operation of High-Power (200 mW) Strained-Layer $Ga_{1-x}In_xAs$/GaAs Quantum-Well Lasers with Emission Wavelengths $0.87 \le \lambda \le 0.95$ μm," *Electron. Lett.* **24**, 1493 (1988).
11. S.E. Fischer, R.G. Waters, D. Fekete, J.M. Ballantyne, Y.C. Chen, and B.A. Soltz, "Long-Lived InGaAs Quantum Well Lasers," *Appl. Phys Lett.* **54**, 1861 (1989).
12. L.E. Eng, T.R. Chen, S. Sanders, Y.H. Zhuang, B. Zhao, Y. Yariv, and H. Morkoç, "Submilliampere Threshold Current Pseudomorphic InGaAs/AlGaAs Buried-Heterostructure Quantum Well Lasers Grown by Molecular Beam Epitaxy," *Appl. Phys. Lett.* **55**, 1378 (1989).
13. D.P. Bour, R.U. Martinelli, D.B. Gilbert, L. Elbaum, and M.G. Harvey, "Operating Characteristics of InGaAs/AlGaAs Strained Single Quantum Well Lasers," *Appl. Phys. Lett.* **55**, 1501 (1989).
14. K.J. Beernink, P.K. York, J.J. Coleman, R.G. Waters, J. Kim, and C.M. Wayman, "Characterization of InGaAs-GaAs Strained-Layer Lasers with Quantum Wells near the Critical Thickness," *Appl. Phys. Lett.* **55**, 2167 (1989).
15. A. Larsson, J. Cody, and R.J. Lang, "Strained-Layer InGaAs/GaAs/AlGaAs Single Quantum Well Lasers with High Internal Quantum Efficiency," *Appl. Phys. Lett.* **55**, 2268 (1989).
16. D.F. Welch, W. Streifer, C.F. Schaus, S. Sun, and P.L. Gourley, "Gain Characteristics of Strained Quantum Well Lasers," *Appl. Phys. Lett.* **56**, 10 (1990).
17. H.K. Choi and C.A. Wang, "InGaAs/AlGaAs Strained Single Quantum Well Diode Lasers with Extremely Low Threshold Current Density and High Efficiency," *Appl. Phys. Lett.* **57**, 321 (1990).
18. A.R. Adams, "Band-Structure Engineering for Low-Threshold High-Efficiency Semiconductor Lasers," *Electron. Lett.* **22**, 249 (1986).
19. E. Yablonovitch and E.O. Kane, "Reduction of Lasing Threshold Current Density by the Lowering of Valence Band Effective Mass," *J. Lightwave Technol.* **LT-4**, 504 (1986).
20. D.P. Bour, D.B. Gilbert, K.B. Fabian, J.P. Bednarz, and M. Ettenberg, "Low Degradation Rate in Strained InGaAs/AlGaAs Single Quantum Well Lasers," *IEEE Photon. Technol. Lett.* **2**, 173 (1990).
21. R.G. Waters, D.P. Bour, S.L. Yellen, and N.F. Ruggieri, "Inhibited Dark-Line Defect Formation in Strained InGaAs/AlGaAs Quantum Well Lasers," *IEEE Photon. Technol. Lett.* **2**, 531 (1990).
22. J. Matsui, "Degradation Behavior of Optoelectronic Devices," *Mat. Res. Soc. Symp. Proc.* **14**, 477 (1983).
23. N. Kobayashi, Y. Horikoshi, and C. Uemura, "Room Temperature Operation of the InGaAsSb/AlGaAsSb DH Laser at 1.8 μm Wavelength," *Jpn. J. Appl. Phys.* **19**, L30 (1980).
24. T.H. Chiu, W.T. Tsang, J.A. Ditzenberger, and J.P. van der Ziel, "Room-Temperature Operation of InGaAsSb/AlGaSb Double Heterostructure Lasers near 2.2 μm Prepared by Molecular Beam Epitaxy," *Appl. Phys. Lett.* **49**, 1051 (1986).
25. C. Caneau, J.L. Zyskind, J.W. Sulhoff, T.E. Glover, J. Centanni, C.A. Burrus, A.G. Dentai, and M.A. Pollack, "2.2 μm GaInAsSb/AlGaAsSb Injection Lasers with Low Threshold Current Density," *Appl. Phys. Lett.* **51**, 764 (1987).
26. A.E. Drakin, P.G. Eliseev, B.N. Sverdlov, A.E. Bochkarev, L.M. Dolginov, and L.V. Druzhinina, "InGaSbAs Injection Lasers," *IEEE J. Quant. Electron.* **QE-23**, 1089 (1987).
27. A.E. Bochkarev, L.M. Dolginov, A.E. Drakin, P.G. Eliseev, and B.N. Sverdlov, "Continuous-Wave Lasing at Room Temperature in InGaSbAs/GaAlSbAs Injection Heterostructures Emitting in the Spectral Range 2.2–2.4 μm," *Sov. J. Quant. Electron.* **18**, 1362 (1988).
28. A.N. Baranov, T.N. Danilova, B.E. Dzhurtanov, A.N. Imenkov, S.G. Konnikov, A.M. Litvak, V.E. Usmanskii, and Yu.P. Yakovlev, "CW Lasing in GaInAsSb/GaSb Buried Channel Laser ($T = 20°C$, $\lambda = 2.0$ μm)," *Sov. Tech. Phys. Lett.* **14**, 727 (1988).
29. J.L. Zyskind, J.C. DeWinter, C.A. Burrus, J.C. Centanni, A.G. Dentai, and M.A. Pollack, "Highly Uniform, High Quantum Efficiency GaInAsSb/AlGaAsSb Double Heterostructure Lasers Emitting at 2.2 μm," *Electron. Lett.* **25**, 568 (1989).
30. A.N Baranov, A.N. Imenkov, M.P. Mikhailova, A.A. Rogachev, and Yu.P. Yakovlev, "Lasers and Avalanche Photodiodes for IR Fiber Optics in the 2–2.5 μm Spectral Range," *Proc. SPIE* **1048**, 188 (1989).
31. S.J. Eglash and H.K. Choi, "Efficient GaInAsSb/AlGaAsSb Diode Lasers Emitting at 2.29 μm," *Appl. Phys. Lett.* **57**, 1292 (1990).
32. F. Karouta, A. Marbeuf, A. Joullié, and J.H. Fan, "Low Temperature Phase Diagram of the $Ga_{1-x}In_xAs_ySb_{1-y}$ System," *J. Cryst. Growth* **79**, 445 (1986).
33. G. Motosugi and T. Kagawa, "Liquid-Phase Epitaxial Growth and Characterization of AlGaAsSb Lattice-Matched to GaSb Substrates," *J. Cryst. Growth* **49**, 102 (1980).
34. W.D. Goodhue, "Using Molecular Beam Epitaxy to Fabricate Quantum-Well Devices," *Lincoln Laboratory J.* **2**, 183 (1989).
35. A. Sugimura, "Band-to-Band Auger Effect in Long Wavelength Multinary III-V Alloy Semiconductor Lasers," *IEEE J. Quant. Electron.* **QE-18**, 352 (1982).
36. N.K. Dutta, "Calculated Absorption, Emission, and Gain in $In_{0.72}Ga_{0.28}As_{0.6}P_{0.4}$," *J. Appl. Phys.* **51**, 6095 (1980).
37. D. Botez and M. Ettenberg, "Beamwidth Approximation for the Fundamental Mode in Symmetric Double-Heterojunction Lasers," *IEEE J. Quant. Electron.* **QE-14**, 827 (1978).

HONG K. CHOI
has been a staff member in the Electronic Materials Group at Lincoln Laboratory since 1983. His current research interest is in developing diode lasers by using a variety of material systems, including GaAs/AlGaAs on GaAs and Si, InGaAs/AlGaAs on GaAs, and GaInAsSb/AlGaAsSb on GaSb substrates. Hong received a B.S. from the Seoul National University, an M.S. from the Korea Advanced Institute of Science and Technology, and a Ph.D. from the University of California at Berkeley, all in electrical engineering. From 1975 to 1978 he worked at the Agency for Defense Development in Korea. He is a member of the IEEE and the Materials Research Society.

CHRISTINE A. WANG
is a staff member in the Electronic Materials Group at Lincoln Laboratory. Her research interests include the development of organometallic vapor phase epitaxy (OMVPE) technology, crystal growth of III-V semiconductors by OMVPE, and the development of semiconductor quantum-well laser structures. Christine received the following degrees from MIT: an S.B. in materials science and engineering, an S.M. in metallurgy, and a Ph.D. in electronic materials. She is a member of Tau Beta Pi, Sigma Xi, and the American Association for Crystal Growth.

STEPHEN J. EGLASH
received a B.S. in electrical engineering from the University of California at Berkeley, and an M.S. and Ph.D. in electrical engineering from Stanford University. While attending school, Steve worked part-time at the Hewlett-Packard Laboratories in Palo Alto, Calif., from 1974 through 1985.

Five years ago, Steve joined Lincoln Laboratory, where he is currently a staff member in the Electronic Materials Group. His research focus is on the use of molecular-beam epitaxy to grow semiconductor materials for the fabrication of electronic and opto-electronic devices.

In 1985 Steve received the Ross M. Tucker Electronic Materials Award from the American Institute of Mining, Metallurgical, and Petroleum Engineers. He is a member of the Materials Research Society, the American Vacuum Society, the IEEE, and Sigma Xi.